 doi:10.20944/preprints202208.0281.v1

Article

Improving Hazardous Gas Detection Behavior with Palladium Decorated Sno2 Nanobelts Networks

Estácio P. de Araújo[1]; Murilo P. Paiva[2]; Kate C. Blanco[3]; Adenilson J. Chiquito[1]; Cleber A. Amorim [4, 2,*]

[1] NanOLaB, Departamento de Física, Universidade Federal de São Carlos—UFSCar, Rodovia Washington Luiz, Km 235 Monjolinho, CP 676, CEP 13565-905 São Carlos, SP, Brazil; estaciopaiva@gmail.com
[2] Programa de Pós-Graduação em Engenharia Elétrica (Mestrado), Instituto de Ciência e Tecnologia - Câmpus de Sorocaba, CEP 18087-180, Sorocaba, SP, Brazil; pulze.paiva@unesp.br
[3] São Carlos Institute of Physics, University of São Paulo—Box 369, 13566-970, São Carlos, SP, Brazil; blancokate@gmail.com
[4] School of Sciences and Engineering, Av. Domingos da Costa Lopes, São Paulo State University (Unesp), 780 Jardim Itaipu, CEP 17602-496 Tupã, SP, Brazil, cleber.amorim@unesp.br
* Correspondence: cleber.amorim@unesp.br; Tel.: (+55 14 3404 4221)

Abstract: The colorless, odorless, and tasteless gases monoxide and carbon dioxide, when present in specific amounts in the air, may either replace oxygen in red blood cells (CO) or increase the respiratory rate causing cardiac arrhythmias (CO_2), leading to death. Commercial sensors take around 8 h to detect levels of CO (50 PPM), causing moderate poisoning. SnO_2 presents controlled interactions with the atmosphere using conductance and vacancy adjustments to capture electrical properties. However, the selectivity of gas detection by SnO_2 can still be improved, thus also increasing the application possibilities. The present study aimed to optimize the sensing of CO and CO2 in SnO_2 using palladium functionalization. The vapor-liquid-solid method synthesized a network of SnO_2 nanobelts decorated with palladium nanoparticles. The sensitivity of the sensors for CO and CO_2 were evaluated, characterizing parameters such as response time, a wide range of CO and CO_2 concentrations, and temperature. In the seventh measurement cycle, the sensor response for different concentrations of gases in consecutive cycles showed a sensitivity of up to 125% for CO in 200s (3 minutes?). Furthermore, we observed increased sensor sensitivity with material doping with nanoparticles from 130 ppm to 1360 ppm in 30 seconds to CO. Conclusion: The results provide a better understanding of the sensitivity of SnO_2 in palladium-decorated nanoparticles, offering insights for detecting low CO concentrations quickly. The behavior of these doped nanosensors showed us the importance of considering them as a practical possibility for detecting these gases of importance to human health.

Keywords: nanobelts; tin oxide; gas sensor; carbon monoxide; carbon dioxide; CO; CO_2

1. Introduction

Tin oxide (SnO_2) has a tetragonal rutile structure belonging to the P42/mnm space group, good crystalline quality, lattice constants of a=b = 4.7399 Å and c= 3.1881 Å, high band gap energy (3.6 eV) and high exciton binding energy (130 meV) at room temperature [1–5]. SnO_2-based gas sensors have been developed for years, mainly those whose conductance is modified due to interactions with the gas atmosphere [6–8]. In recent years, control of the electrical properties of SnO_2 nanobelts (NB) has attracted significant attention [9–11]. Especially, SnO_2-based NB is particularly useful due to conductance tuning, possibly due to the vacancy control [12]. Additionally, these materials have higher length-to-diameter and surface-to-volume ratios than bulk materials. SnO_2 NB are one-dimensional and have attracted attention thanks to their unique properties and various special nanostructures. SnO2 is a strong candidate for future transistors, piezoelectric devices, and solar cells [13]. Furthermore, the high sensibility to toxic and combustible gases can

 doi:10.20944/preprints202208.0281.v1

be highlighted, accelerating studies on SnO_2 gas sensors in different geometries, such as thin films, heterojunctions, nanoparticles, and NB [14].

Nanobelts are synthesized by various techniques [15–18] and have been widely applied as gas sensors. Thus, the new generation of gas sensors will have to present characteristics such as excellent cost-benefit ratio, high sensibility, and selectivity, and being a stable [19–21]. The selectivity of detection of gas sensors based on transparent conducting oxide (TCOs) is still the subject of significant challenges for the development of sensory systems used in environmental monitoring, as well as industrial safety applications.

The oxide NB metal functionalization, in addition to presenting economic advantages, is also a powerful way to improve the sensibility and selectivity of the NB [14]. According to Chan et al., the improvement obtained through functionalization by metallic nanoparticles can be understood from different views, such as manipulation of the acid-based properties of the NB surface, change in donor density, catalytic promotion, and extension of the electron depletion region at the junction metal-semiconductor [22]. SnO_2 NB have already been functionalized with different catalytic nanoparticles such as SiO_2, palladium, copper, platinum, and Lysine to improve the selective detection of other analytes, including acetone, and sulfur dioxide, nitrogen dioxide, carbon dioxide, and hydrogen [23–27].

The detection process in SnO_2 NB is based on the change in the material's conductivity through the difference in the concentration of electrons caused by adsorption and desorption of the analyte (gas). When SnO_2 comes into contact with the analyte, its molecules react with the adsorbed oxygen anions. These charges become free and can be promoted back to the conduction band, causing the sensor resistance to change. Kalmakov *et al.* showed that in the presence of carbon monoxide, SnO_2 reacts with pre-absorbed species such as $O^-_{(s)}$ and $O^{2-}_{(s)}$, reducing the concentration of oxygen on the surface, donating the few electrons to the volume of the material, resulting in an increase in conductivity, which depends on the CO concentration [6]. The surface condition plays a crucial role in CO_2 detection. In an atmosphere rich in nitrogen, commonly used as a carrier gas, oxygen molecules are excluded from forming oxygen species such as O_2^-, O^- and O^{2-} in the region close to the surface [28,29]. CO_2 is a weak reducing gas, poorly ionized when it reacts with oxygen vacancies. The electron gain, due to the presence of CO_2, creates a change in the carrier concentration, thus decreasing its general resistance, as observed in several works [4,13,24].

In recent years, due to the increase in the temperature of the planet - global warming, gases such as CO_2 and CO have been highlighted. There are several myths about how these gases are obtained and the dangers they can cause. Both gases are present in the environment and have different compositions and are generated through various chemical reactions. Additionally, CO_2 and CO do not cause the same effects in the human body, although they are both toxic. CO can be produced through any incomplete combustion of fuel, usually associated with a low amount of oxygen. However, this gas is not formed naturally; it can be formed through boilers, combustion engines, heaters in general, fireplaces, etc. As can be seen, the generation of this gas is associated with human behavior and, as it is so dangerous, it can cause many problems to human beings, including leading to death. According to the Occupational Safety and Health Administration (OSHA), concentrations above 200 ppm can cause headaches, fatigue, and nausea after 2-3 hours of continuous exposure. Concentrations above 600 ppm can already lead to death.

On the other hand, CO_2 is also a toxic gas found in the atmosphere at a concentration of approximately 400 ppm, while the limited tolerance is around 3900 ppm. This gas can be generated, in addition to those ways mentioned for CO, but also through fermentation processes. Due to the danger presented by these gases, their monitoring becomes essential, not only for safety but also for the quality of life, since even at low concentrations, there will be some adverse effects.

 doi:10.20944/preprints202208.0281.v1

In the present work, NB made of pure SnO_2 and decorated with palladium was synthesized by vapor-liquid-solid (VLS) methods, forming a network of nanobelts. Pd nanoparticles were deposited after NB growth by thermal evaporation. The grown samples presented a simple design and easy direct application as gas sensors without having to go through a photolithography process to define electrodes. In this way, we believe we have a simple and easy-to-apply device. Both devices were tested at different temperatures, 50 and 75 ^{o}C. Their response was obtained for various concentrations of both CO and CO_2. A comprehensive study of these gases' detection mechanisms was also presented. Finally, the results showed a relatively low concentration of the studied gases compared to SnO_2-based sensors in the literature, which the vast majority work under high temperatures. Furthermore, our devices showed a rapid response and recovery after exposure to the analytes studied.

2. Materials and Methods

SnO_2 NBs were grown using the method proposed by Wagner et al., Vapor-Liquid-Solid [15] and also described by Araújo et al. [30]. This method consists of depositing a thin metallic layer (15 Å) on a Si/SiO_2 substrate, which will serve as catalyzed nanoclusters. These clusters are used as preferential sites for adsorption of vapor phase components, leading to a one-dimensional growth of the structures. 0.1 g of tin powder (Aldrich, purity>99.99%) was placed in an alumina crucible and placed in the center of a tubular reactor (Lindberg blue M). The system is heated to 950 °C at a rate of 20 °C/min and held at this level for 50 min. The vapor generated by the precursor powder is carried by an Argon/Oxygen gas mixture (15/8 sccm - Mass Flow MKS 1149) throughout the synthesis time; the pressure is kept constant at around 350 mbar; a schematic profile of the growth process is shown in **Figure *1***a. The material as grown is shown in **Figure *1***b; after growth, a palladium thin layer (~ 5nm) was evaporated onto the as-grown nanobelts; this evaporation presented a dark appearance in contrast to a lighter region shadowed by the sample holder used in the thermal coater system. (**Figure *1***c). After evaporation, these samples underwent heat treatment, 300 ^{o}C for 30 min, to produce the metallic nanoparticles (**Figure *1***d).

The material as-grown was analyzed according to scanning electron microscopy (SEM, JEOL JSM 6510, operated at 20 kV), X-ray diffraction (XRD, Rigaku D/max-2500, Cu-Kα radiation), and Raman Spectroscopy (HR800 Evolution micro-Raman spectrometer, Horiba-Jobin-Yvon, laser diode operating at 532nm). **Figure *1***e shows an SEM image of the samples as grown. At the bottom is a nanobelt with a catalytic Au nanoparticle at the tip, confirming the VLS growth mechanism. The composition of the as-grown material can be evidenced through EDX measurements. These results show that the nanobelts are composed of Sn and O (**Figure *1***d). The crystalline phase of the synthesized samples was analyzed by X-ray diffraction. **Figure *1***g shows the spectrum obtained at room temperature for pure SnO_2 nanobelts. The results indicate that the samples presented a tetragonal structure of the rutile type (JCPDS: 41-1445) belonging to the P42/mnm space group [1,3]; the nanobelts showed an excellent crystalline quality. Finally, **Figure *1***h shows the Raman spectrum of the SnO_2 nanobelts. We can observe that the spectrum of the samples showed bands centered at 474, 632, and 775 cm^{-1}, corresponding to three active Raman vibration modes (E_g, A_{1g}, and B_{2g}), respectively [31,32]. The results showed a typical characteristic of the rutile phase of SnO_2 nanobelts in agreement with the XRD measurements.

Preprints (www.preprints.org) | NOT PEER-REVIEWED | Posted: 16 August 2022 doi:10.20944/preprints202208.0281.v1

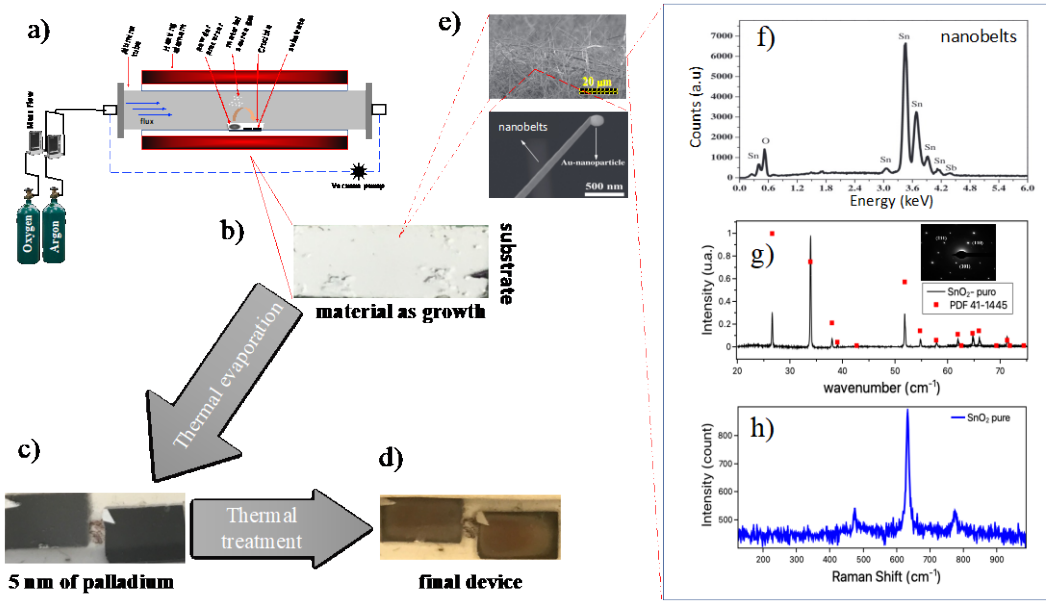

Figure 1. Schematic representation of the nanobelts growth configuration, decoration with nanoparticles, and structural characterization: (a) profile of the tubular oven reactor with the main items for the growth of nanobelts; the material as grown on Si/SiO_2 substrate is shown in panel b); some as-grown samples went through a process of deposition of palladium nanoparticles (5 nm) and it is possible to observe a white region due to the sample holder inside the thermal coater system; in panel d) the substrates with the nanobelts after the heat treatment are shown Samples shown in panel b) were characterized by morphological and structural analysis: in panel e) is depicted a SEM image showing a network of as-grown nanowires, highlighting a single nanobelt of SnO_2 showing the Au nanoparticles, typical of VLS growth (immediately below figure); in panel f) the EDX spectrum of the as-grown samples is shown; and finally in panels g) and h) the XRD pattern of the as-synthesized SnO_2 nanowires and room-temperature Raman spectrum of SnO_2 nanobelts are shown.

Once the material was grown, it did not need to undergo to any photolithography process to define the metallic electrodes. We emphasize that this is extremely important because it allows the development of devices quickly and at a lower cost when compared to those that require photolithography. Such types of devices were already used in previous works, as seen in [30,33]. These devices were built in a metal/NB/metal architecture, where the metallic electrodes were commercially Test Probes Contact Pins type, connected directly to the gas detection chamber.

The target gases in this study were CO_2 (40-800 ppm; 99.99% purity) and CO (70-1300 ppm; 99.99% purity). The different desired concentrations were obtained by purging the gas in an airtight chamber of approximately 50 mL with a known volume of nitrogen gas determined by a mass flow controller (Mass Flow MKS 1149). The concentration obtained is a ratio between the nitrogen fluxes (background gas) and the target gas (CO and CO_2), in addition to the respective molar masses of these gases. That's why the concentration values were so different from each other. The final gas flow was maintained at a rate of approximately 50 sccm. Teflon O-rings were used in the metal joints of the gas chamber to seal it against gas leaks. Sensor experiments were conducted under nitrogen flow with different conditions: *i.* pure SnO_2, different concentrations of target gases, temperatures of 50 and 75 °C; *ii.* SnO_2 with palladium nanoparticles, different concentrations of target gases, and temperatures of 50 and 75 °C.

 doi:10.20944/preprints202208.0281.v1

The sensor response, and sensibility, reflects the concentration of the target gases, and this can be monitored by recording the changes in the conductivity of the SnO_2 nanowire network. The sensibility of the sensors was calculated as follows:

$$S(\%) = \frac{\Delta R}{R_0} = \frac{R_0 - R_E}{R_0} \times 100, \quad (1)$$

where the E-index refers values resistance and current under gas exposure, while the 0-index refers to the reference resistance/current values (baseline) which were obtained when the sensor is exposed to nitrogen flow only. The eq. (1) has two exciting aspects depending on the exposed gas. When exposed to CO_2, a reducing gas (it will transfer electrons to the nanobelts' system), it will increase the sample current (S > 0). On the other hand, when exposed to an oxidizing gas such as CO, electrons will be withdrawn from the nanobelts' system, decreasing the sensor current (S < 0). In this work, we define the response time where the sensor reaches 90% of the maximum change after exposure to the gas samples. Thus, recovery time was defined as the time required to recover 10% of the initial baseline value after exposure to the target gas [34].

3. Results

Figure 2b shows the characterization configuration of the target gas sensors. All measurements were made under nitrogen gas as a background, to which the target gases were mixed. The measured concentrations were obtained using a mass flow controller of one cubic centimeter per minute (sccm). The detection chamber has a volume of approximately 25 cm^3; coupled to it there is a heater where the working temperature can be controlled from room temperature to 300 ^oC. Attached to the detection chamber, two connection pads make electrical contact with the NB network. This process demonstrates the practicality and speed of building and testing gas sensors. Current-time characterization was performed by applying an electrical voltage of 5.0 V and monitoring the electrical current using a Keithley 6517-B. Finally, a sketch model of the applied voltage is shown at $t_0 = 0$; after a specific time, the target gas is inserted into the camera, and the sensor responds, as shown in the red curve. The figure refers to the result for an oxidizing gas (CO). After $t_1 > 0$, the target gas is switched off, and the sensor behavior is restored.

The setup described above was used to obtain the curves shown in Figure 2b and Figure 2c. Figure 2b shows the sensibility curve, obtained from equation (1), at room temperature for the CO sample. The concentrations studied were extremely high, above 1600 ppm. The system was tested for these values because they were the only ones that offered the sensor response at room temperature. Figure 2b shows the curves obtained when the target gas is carbon dioxide in concentrations between 960-3000 ppm. The concentration obtained is a ratio between the nitrogen fluxes (background gas) and the target gas (CO and CO_2), in addition to the respective molar masses of these gases. That's why the concentration values were so different from each other.

Preprints (www.preprints.org) | NOT PEER-REVIEWED | Posted: 16 August 2022 doi:10.20944/preprints202208.0281.v1

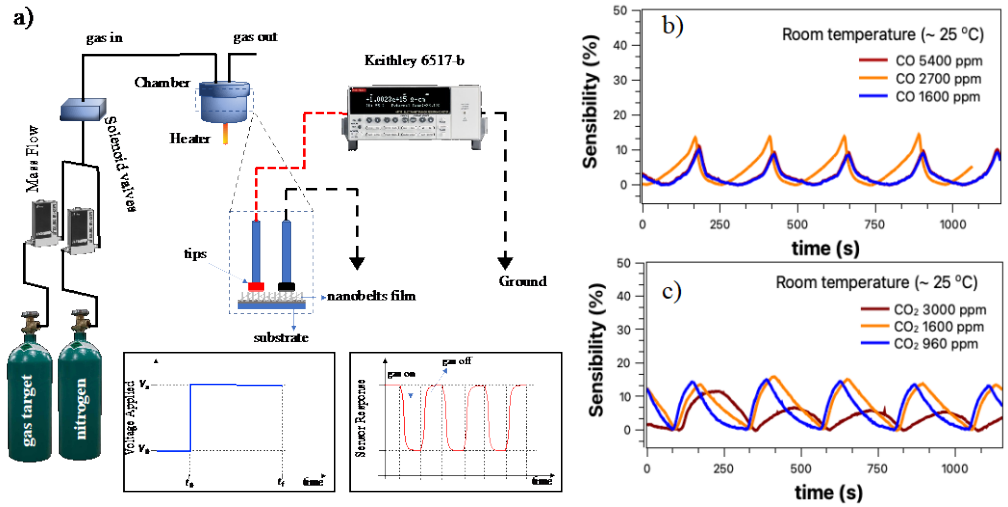

Figure 2. Schematic representing the setup configuration used for gas detection, including gas cylinders, mass flow controllers, solenoid valves, detection chamber, test leads, the Keithley 6517-B electrometer, and a representative response curve sensor (oxidizing gas); in b) the sensor response for the CO target gas at different concentrations and in c) the results for CO_2.

There are two essential aspects of Figure 2b and Figure 2c: *i.* the sensor responses of both curves are practically the same, although with a different shape; *ii.* The result obtained when the target gas was CO was expected to have a negative sensibility (eq. 1) because it is an oxidizing gas that steals electrons from the sensor surface (this process is described below). To obtain any signal beyond the background, the gas flow inside the detection chamber needed to be above 100 sccm. Indeed, when the target gas is CO_2, there is some charge transfer to the SnO_2 nanobelts film. However, this transfer is irrelevant since the response obtained for a concentration of 3000 ppm is lower than for the other concentrations Figure 2c. Additionally, when the target gas was CO, the sensibility was expected to be negative (eq. 1), as the response current is smaller than the background current, and this was not observed Figure 2b. We believe that the response observed in both cases is due to turbulent flow (high sccm's) inside the chamber, which is more likely related to a temperature variation or surface cleaning than to the presence of gas.

The results presented in Figure 2b-c led us to two questions: *i.* at what temperature can we have a correct answer for the gas sensors; *ii.* And under which conditions we will have the lowest sensor operating temperature. Figure 3 presents the sensibility curves obtained for the target gases CO and CO_2, for temperatures of 50 and 75 °C. All measurements were performed under a constant flow of nitrogen for approximately 120 seconds; after this period, the valve with the target gas is opened for approximately 30s and then closed. Two cycles were obtained, the second cycle being more stable than the first.

Preprints (www.preprints.org) | NOT PEER-REVIEWED | Posted: 16 August 2022 doi:10.20944/preprints202208.0281.v1

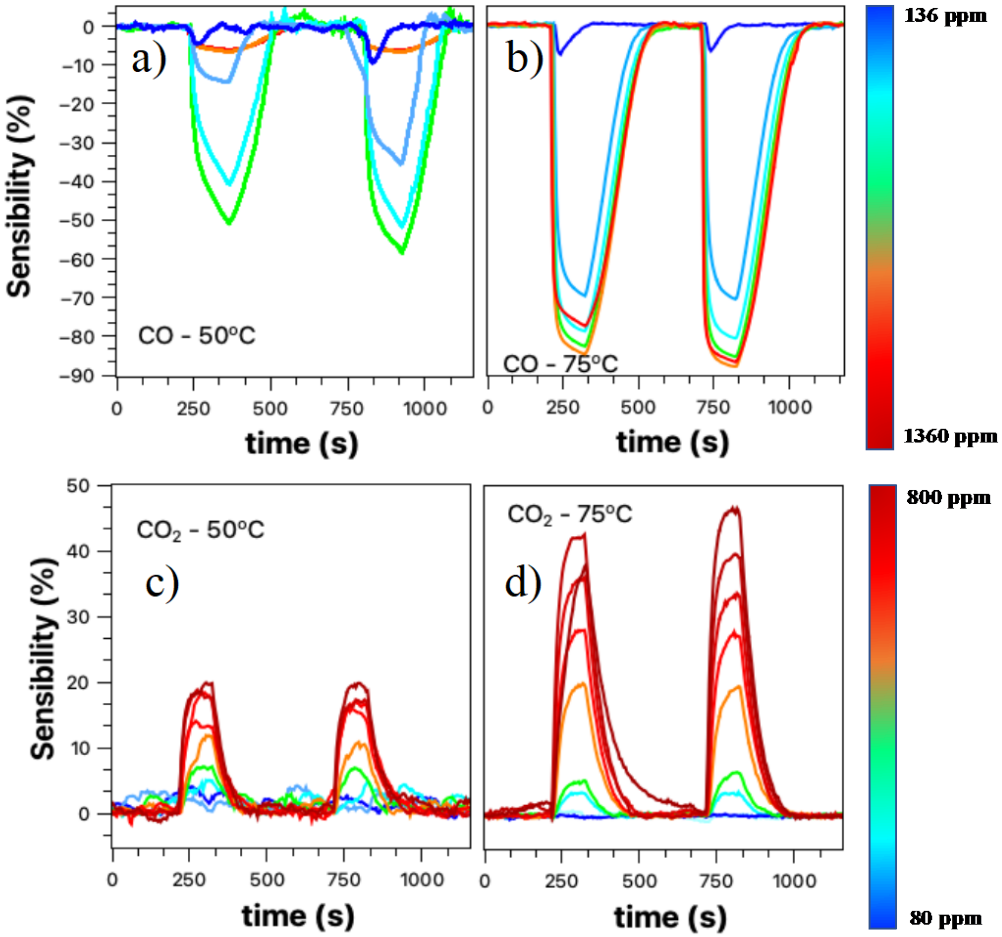

Figure 3. Panels a and b show sensor sensibility for CO gas at temperatures 50 and 75 °C, respectively; In panels c) and the sensor sensibility for O_2 gas is shown at 50 and 75 °C, respectively.

The CO sensor response at 50°C (Figure 3a) shows a response with an increasing concentration of the target gas. It is noteworthy that the negative sign of the sensibility is kept only to indicate the typical response of an oxidizing gas. As we increase the concentration, the sensor response tends to increase, except for values up to 1300 ppm. Such behavior can be attributed to sensor saturation, although in this case, it was expected that the observed sensibility value would be close to 50%. Another explanation may be related to the one presented above. For these CO concentrations, the flux inside the detection chamber is relatively high to the point of lowering the working temperature and having a cleaning effect on the nanobelts network surface. Figure 3b shows the CO gas sensor response for a temperature of 75 °C in a concentration range between 136-1360 ppm. There is an evident improvement in the sensor response with increasing concentration of the target gas; however, for high concentrations, there is still a saturation region. The entire process of detecting the SnO_2 nanobelts film for carbon monoxide will be discussed later.

Figure 3c-d presents the results for the CO_2 target gas (80-800 ppm) at 50 and 75 °C, respectively. We can see that the response practically doubled with the increase in temperature; in addition, there was an improvement in the resolution of the sensor, especially when we look at the second cycle. For the temperature of 50 °C, there is a response for the target gas; however, there is no direct relationship between the response and the increase in concentration. This effect is overcome when the temperature is 75 °C, when the definition of the response becomes evident. This process will be discussed later.

The results presented in Figure 2 and Figure 3 showed that although the SnO_2 nanobelts network could detect the presence of the analyte under study, it was impossible to

Preprints (www.preprints.org) | NOT PEER-REVIEWED | Posted: 16 August 2022 doi:10.20944/preprints202208.0281.v1

have a direct relationship and resolution, as found in the literature [4,6,35]. Increasing the working temperature (room temperature, 50 °C, and then 75 °C) improved these aspects, but the device still showed a low resolution. Like other authors who studied SnO_2 as an active layer for detecting gases such as CO and CO_2, we decorated the nanobelts films with palladium nanoparticles [24,36–38].

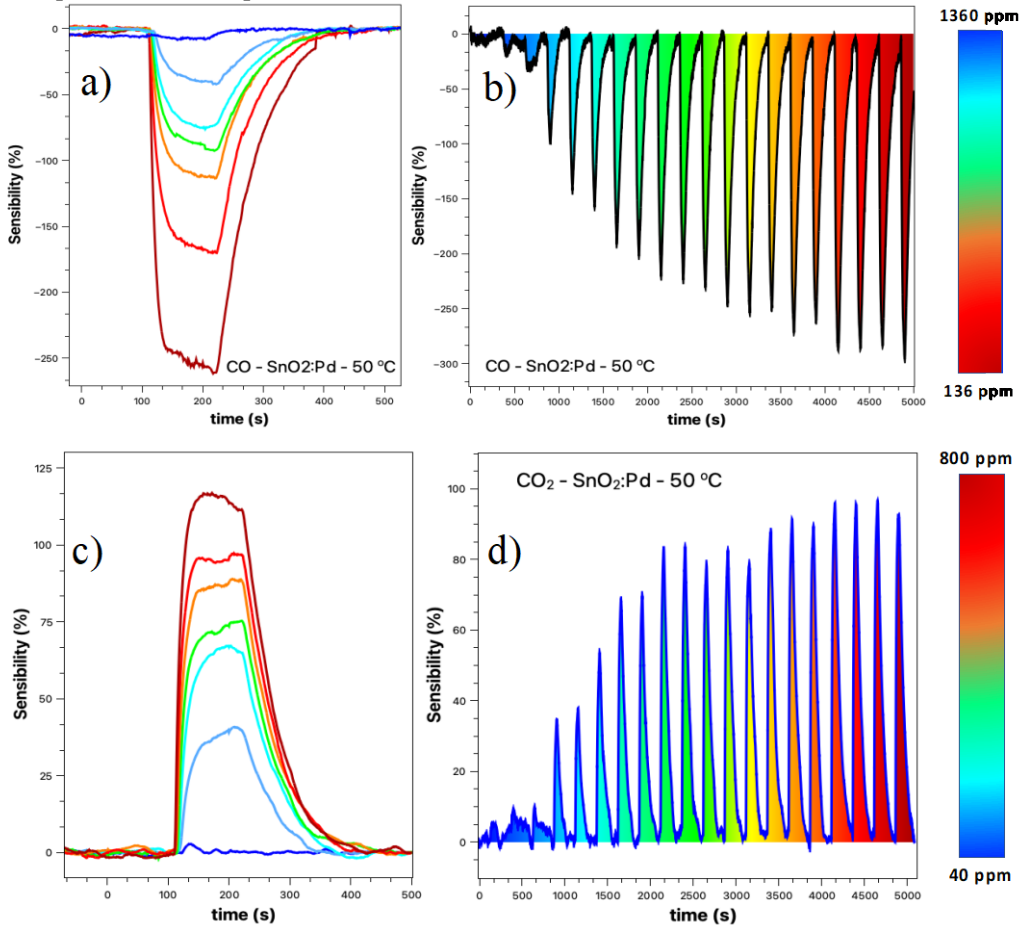

Figure 4. a) Sensor response for different CO concentrations within the 136-1360 ppm; b) Similar measure to the previous one. However, the concentration was gradually increased after each cycle; in c) we have the sensitivity for different CO_2 concentrations between 40-800 ppm, in d) a gradual measure of the sensitivity for the described range of concentrations. All under the same applied voltage value of +5 V.

To improve the properties of SnO_2 nanobelts-based sensors at a temperature as close as possible to room temperature, we decorated the nanobelts films with palladium nanoparticles, as described in section **2**. Responses were measured for both CO and CO_2 over a wide concentration range. Figure 4 shows the result for these samples for 50 °C (other temperatures were not tested because we are only interested in the working temperature closest to the ambient). Figure 4a, shows the sensibility curve at different concentrations. We observed that there is a better definition in the sensor response, that is, there is no more overlap between the response curves, when compared to the results presented in Figure 3a-b, with the maximum response being more than doubled. Figure 4b shows the detection spectrum of the SnO_2 nanobelts film sensor, taken by increasing the concentration at each cycle. There is a low background response when the concentration is below 210 ppm (third "peak" from left to right (Figure 4b)). From this value onwards, the response becomes more prominent and tends to increase with increasing CO concentration, and there is a saturation tendency for concentrations above 1150 ppm (17th peak).

Similarly, we tested the same device for the CO_2 target gas; Figure 4c shows that the relative response increased about sixfold when compared to that shown in Figure 2c, for

Preprints (www.preprints.org) | NOT PEER-REVIEWED | Posted: 16 August 2022 doi:10.20944/preprints202208.0281.v1

the device without the palladium nanoparticles. The increase was 2.5 times higher when compared to the sample without the nanoparticles, but at 75 °C. Additionally, we observed an improvement in the sensor resolution, with a more straightforward response for different concentrations used. Figure 4d shows the response obtained for the CO_2 target gas at a concentration of 40 – 800 ppm with steps of 40 pm. For concentrations below 120 ppm, the response is very low and close to the background values. However, for values above this, the response becomes clearer, tending to saturation for values above 680 ppm. In the next section, we will discuss, in more detail, why the sensor is sensitive to these two gases and why the presence of nanoparticles improves the sensibility and resolution of the sensor.

Some parameters are extremely important to characterize a sensor, such as sensitivity (here defined as the change in the input parameter required to produce a standardized output change) and the response and recovery time of the sensor. These parameters can place the device as a strong candidate for future applications. Figure 5 compiles all this information regarding the characterization parameters of the CO and CO_2 sensor based on SnO_2 nanobelts film.

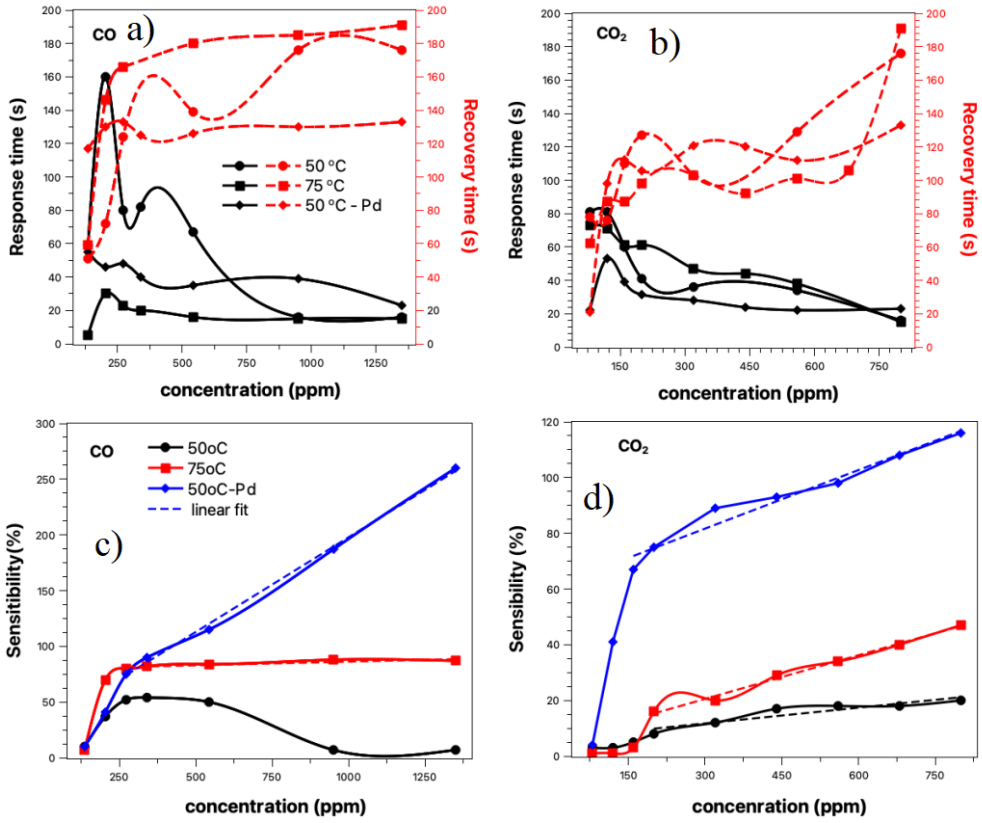

Figure 5. Response time and recovery time for CO and CO_2 gas sensor, a) and b), respectively; in c) and d) we have the sensitivity vs concentration graphs for CO and CO_2, respectively. All the results presented were taken for 50 °C with and without palladium nanoparticles and 75 °C. Legend: (■) 50 °C; (●) 75 °C; (◆) 50 °C – Pd nanoparticles.

Figure 5 shows the results for response and recovery time, sensibility *vs.* concentration obtained for the curves shown in Figure 3 and Figure 4. The solid lines represent the response time, and the dashed lines the recovery time (see Figure 5b and c). We have two comparisons to be carried out between the two temperatures studied and between the sensor with and without palladium nanoparticles. The response time obtained was between 160-20 s. In all cases, the response time tends to decrease with the gas increasing concentration. For a temperature of 50 °C (solid line-circle), there is an increase in response time up to approximately 350 ppm; from this point on, there is a considerable drop, tending to a constant response time for concentrations above 800 ppm. Similar behavior was

Preprints (www.preprints.org) | NOT PEER-REVIEWED | Posted: 16 August 2022 doi:10.20944/preprints202208.0281.v1

observed for sensor response at 75 °C (solid line-square), however, a shorter response time was observed for this case, and from 200 ppm, no significant change was recorded. When we compare the two temperatures studied, we can observe that the response time is influenced by them for concentrations below 800 ppm; for values above that, both converge.

On the other hand, the presence of nanoparticles makes the response time of the sensors shorter when compared to the device without the nanoparticles for the same temperature. For values above 800 ppm, the value is close to the other cases but getting slightly higher. The influence of temperature and nanoparticles decorating the nanobelts film is best observed in the recovery time of the sensors (red dash lines). The best recovery times were observed for the nanobelts film with palladium nanoparticles, with a practically constant value with increasing concentration (~ 120 seconds). When comparing sensor operation at 50 and 75 °C, the latter showed a slightly longer recovery time when comparing the exact gas concentration. The effect of temperature and the sensor with nanoparticles was also evident in the response time of the sensor when exposed to CO_2 gas (see Figure 5b). Above 150 ppm the response time was practically constant at 20 seconds, half the response time compared to CO gas. Additionally, the recovery time was not influenced by the presence of nanoparticles nor by the increase in temperature. Here we define the response time when the sensor reaches 90% of the maximum observed response. In cases involving toxic gases, like the ones we are studying, often the response time must be the one in which the sensor reaches 50% of the maximum value. In this context, the times observed in this work presented a fast response, being very useful in alarm situations where the complete response is unnecessary.

Table 1 - Table referring to the parameters for adjusting the curves shown in Figure 5c and Figure 5d.

	CO				CO_2		
Temperature	*a*	*b*	R^2		*a*	*b*	R^2
50 °C	-	-	-		6,09	1.88×10^{-2}	0.86
75 °C	79.7	$6,56 \times 10^{-3}$	0.79		4,81	5.24×10^{-2}	0.99
50 °C-Pd	27.9	$1,70 \times 10^{-1}$	0.99		60,63	7.00×10^{-2}	0.96

Figure 5c-d presents the results for sensibility *vs.* concentration, this information shows us how sensitive the sensor can be. Except for the response for the CO sensor at 50 °C, all other measurements showed an improvement in sensibility with increasing gas concentration. A linear response was observed for concentrations above 250 ppm for CO gas and above 150 ppm for CO_2, respectively. The relationship between sensitivity and concentration follows a linear fit ($S = a + b \cdot C$), where a is the intercept of the y-axis; here, it does not have much meaning; b is the sensitivity growth rate with concentration (%/ppm), and C is the target gas concentration. Table 1 shows the values obtained for this adjustment under different experimental conditions. The presence of nanoparticles improved the response rate for both gases, with an increase of 26 times for CO and approximately 4 times for CO_2, respectively.

4. Discusions

All curves based on the change in sensor resistance when exposed to target gas can be divided into three phases: stabilization → adsorption/response → recovery. The surface of the nanobelts plays a crucial role in the response of the gas sensor based on metal oxides. As already discussed in another work [28–30]; Tin oxide is one of the most studied n-type semiconductor TCOs for gas sensors. Its detection mechanism is explained based on the change in electrical conductivity, which occurs through the chemical interaction of gas molecules with the oxide surface [39]. It is expected that no oxygen particles will act in the detection chamber since the sensor is continuously exposed to the background gas (Nitrogen). This leads us to form oxygen species like O_2^-, O^- and O^{2-}, near the surface

Preprints (www.preprints.org) | NOT PEER-REVIEWED | Posted: 16 August 2022 doi:10.20944/preprints202208.0281.v1

of the nanobelts [4]. In the presence of the background gas, lesser electrons get enough energy to jump into the conduction band and travel across the junction while holes are left behind. There will be an accumulation of charges at the interface, forming an intermediate spatial charge layer. Thus, the gas sensor will not change resistance when its surface is saturated with nitrogen. As a result, a depletion region is formed. Under the atmosphere of the gas, the acceptor or donor electrons are adsorbed on the surface of the metal oxide, resulting in a change in the material's conductivity. The conductivity of the TCOs gas sensor depends on the charge transfer mechanisms between the adsorbed gaseous species, as well as the surface reaction with the gas. Figure *6* shows the charge transfer on the sensor surface, as well as a diagram representation of the proposed bifunctional detection mechanisms, both for the effect of oxidizing gases and for reducing gases [40].

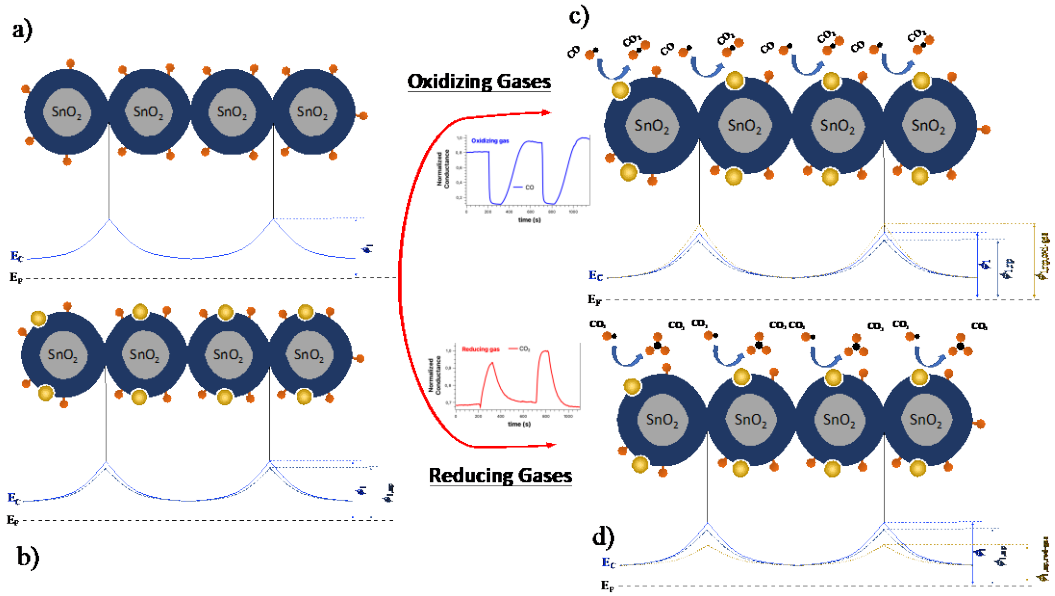

Figure 6 – Schematic illustration of the chemical reactions on the surface of the nanobelts and the respective band diagram: panel a) network of nanobelts with oxygen molecules adsorbed on the surface of the nanobelts; in panel b) Nanobelts network with palladium nanoparticles; in c) chemical reactions involving CO gas, on the left the conductance response; while in d) chemical reactions involving CO_2 gas, on the, left the conductance response.

In our study, we have a SnO_2 nanobelt network which can be described by the energy band theory. Figure *6*a represents this band configuration for this SnO_2 nanobelts network, where the contact point between two nanobelts has the same behavior as a grain boundary structure. These interconnected NB form larger aggregates connected by these junctions. Figure *6*b illustrates the depletion region and the pre-adsorbed oxygen molecules on the surface of SnO_2 and palladium nanoparticles (SnO_2-Pd). The Pd nanoparticles act as catalysts accelerating the dissociation of oxygen molecules, increasing the flow of oxygen ions adsorbed on the NB surface. The more oxygen ions adsorbed on the surface of the SnO_2, the more detection sites there will be, leading to increased sensibility. Depending on the type of gas detected (oxidizing or reducing), the response will increase or decrease the material's conductance. Figure *6*b this was represented by a decrease in the potential barrier. Additionally, SnO_2 has an electron affinity of 4.5 eV, while palladium has a work function of 5.5 eV. Thus, when Pd NPs contact the nanobelts, electrons flow from the SnO_2 to the nanoparticles. A depletion region, or a Schottky barrier, will be formed between both materials [36,41]. Under these conditions, when molecules of a reducing gas (Figure *6*c), for example, interact with pre-adsorbed oxygen electron, they return to the Pd-SnO_2 nanobelts and reduce this Schottky barrier, increasing conductivity. On the other hand, when an oxidizing target gas is adsorbed on the nanobelts network,

 doi:10.20944/preprints202208.0281.v1

the adsorbed oxygen combines with the electrons on the material's surface, increasing the electronic surface barrier. This creates a large amount of positive charge at the material interface. A space charge layer will be formed between the negative charge and the positive charge resulting in a potential barrier around the junctions of the SnO_2 nanobelt network. When electrons in the conduction band are transferred from one nanobelts to another, the junction potential barrier must be overcome.

In the presence of O_2 we have a different detection mechanism. The O_{ads}^- species is found as the primary type of species absorbed at temperatures above 200 °C. In this case, the CO gas interacts with O_{ads}^- and tends to release electrons in the conduction band and thus decreasing the conductance of SnO_2, as observed by different authors [42–44]. The equations below show the chemical reactions in this situation [40].

$$CO + O_{2,ads}^- \rightleftharpoons CO_{2.gas} + e^- \quad (2)$$

$$CO + 2O_{ads}^- \rightleftharpoons CO_3^2 \rightleftharpoons CO_{2.gas} + O_{ads}^- + e^- \rightleftharpoons CO_{2.gas} + \frac{1}{2}O_2 + 2e^- \quad (3)$$

The result of eqs. 2 and eq. 3 shows that the sensor signal tends to decrease in the presence of O_2, as observed by Suematsu et al. and Hahn et al. [40,45,46]. In general terms, the model described above works by reducing the concentration of oxygen on the nanobelts surface by donating some electrons to the conduction band. Resulting in an increase in conductivity, which depends on the concentration of CO. This behavior is contrary to what we observed in Figure 3a-b and Figure 4a-b. In this study, the working temperatures were close to the ambient temperature. Furthermore, there is the possibility of traces of water vapor, both in the gas and background gas. Thus, we believe that the equation that describes the chemical reaction during the detection mechanism is best represented by [40]:

$$CO + HO_{ads} \rightleftharpoons HCOO_{ads} \rightleftharpoons CO_2 + CH_{ads}$$
$$HCOO_{ads} + HO_{ads} \rightleftharpoons H_2CO + 2O_{gas} \quad (4)$$

The eq. (4) leads the sensor to decrease the conductivity, as observed in our case shown in **Figure 3**a-b and **Figure 4**a-b, and also observed by [43].

D. Wang et al. showed how the CO_2 detection mechanism in SnO_2 can be. The CO_2 molecules are adsorbed on the OH^- groups pre-adsorbed on the surface of SnO_2 with the adsorption of C (in CO_2) on the surface-O bridge in the SnO_2 lattice. The adsorption of the O atom on the surface-Sn site. The results show that the CO_2 molecule reacts with O from the OH^- pre-adsorbed on the SnO_2 surface, which promotes the formation of the CO_3 ion and the dissociation of the OH^-. This process can be expressed as:

$$SnO_2 + (OH)_{ads}^- + CO_{2(gas)} \rightarrow SnO_2 + (CO_3)_{ads}^{2-} + H_{ads}^+ \quad (5)$$

The gain of electrons from the gas causes a change in the carrier concentration, increasing the sensor's conductivity. This behavior agrees with what we observed (inferior insert in Figure *6*) and is also observed in other works [24,28,47].

Additionally, we can discuss the device response and recovery times (Figure 5a-b). With the different adsorbent sites and defects, we can expect different mechanisms of oxygen desorption, which contributes to a longer response time until the system reaches stability. Furthermore, the operating condition of the devices, close to ambient temperature, also plays an essential role in longer response times [48]. Araujo *et al.* demonstrated the influence of the applied electric field on the response and recovery time of SnO_2-based sensors. In this case, there is a higher density of electrons that becomes available after cutting off the flow of the target gas due to a thicker depletion layer. When the gas flow is interrupted, there is a condition that facilitates a greater oxygen uptake [30]. Wen-Chieh

Wang *et. al.* showed that the response time in a hazardous sensor is related to the interactions of the gas with the surface. And these interactions depend more on the effect of temperature than on different concentrations of the target gas (Figure 5a-b) [49].

5. Conclusions

In summary, the results presented showed a device based on a network of SnO_2 nanobelts, grown by the VLS method, promising for detecting hazardous gases. This is due to building the device quickly and without the need for photolithography processes, eliminating the need to use a clean room. We could show a wide detection range for both CO and CO_2, values below concentrations that could present a health risk. Additionally, the responses for both gases studied were more significant than 50% for CO and 20% for CO_2, respectively. These results were improved by increasing the temperature from 50 to 75 °C by almost twice. Decorating the devices with palladium nanoparticles improved not only the sensor's response but also its resolution. In this situation, it was possible to observe that the responses reached 250% for CO and 120% for CO_2, respectively. Furthermore, we found that both the response time and the recovery time are low enough to be applied as detectors for the presence of these hazardous gases. Finally, we discuss the models applied to explain the detection mechanisms of both target gases.

Supplementary Materials:

Author Contributions: Conceptualization, C.A.A. and K.C.B.; methodology, E.P.d.A., M. P. P. and C. A. A; writing—original draft preparation, C.A.A. and K.C.B.; writing—review and editing, A.J.C., E.P.d.A., M. P. P., C.A.A. and K.C.B.; supervision, C.A.A, A.J.C. ; funding acquisition, A.J.C. and C. A. A. All authors have read and agreed to the published version of the manuscript.

Funding: This research was funded by FAPESP, grant number 2019/18963-6 and CNPq 305656/2018-0;

Acknowledgments: The authors are grateful for institutional support from the Department of Biosystems Engineering at São Paulo State University (UNESP), the Department of Physics at the Federal University of São Carlos (UFSCar) and the postgraduate program in Electrical Engineering (PPGEE/UNEPS).

Conflicts of Interest: The authors declare no conflict of interest.

References

1. McCarthy, G.J.; Welton, J.M. X-Ray Diffraction Data for SnO 2 . An Illustration of the New Powder Data Evaluation Methods. *Powder Diffr.* **1989**, *4*, 156–159, doi:10.1017/S0885715600016638.
2. Viana, E.R.; Ribeiro, G.M.; de Oliveira, A.G.; González, J.C. Metal-to-insulator transition induced by UV illumination in a single SnO 2 nanobelt. *Nanotechnology* **2017**, *28*, 445703, doi:10.1088/1361-6528/aa871a.
3. Costa, I.M.; Colmenares, Y.N.; Pizani, P.S.; Leite, E.R.; Chiquito, A.J. Sb doping of VLS synthesized SnO 2 nanowires probed by Raman and XPS spectroscopy. *Chem. Phys. Lett.* **2018**, *695*, 125–130, doi:10.1016/j.cplett.2018.02.014.
4. Yuliarto, B.; Gumilar, G.; Septiani, N.L.W. SnO2 nanostructure as pollutant gas sensors: Synthesis, sensing performances, and mechanism. *Adv. Mater. Sci. Eng.* 2015.
5. Sheng Pan, S.; Fung Yu, S.; Xia Zhang, Y.; Yuan Luo, Y.; Wang, S.; Min Xu, J.; Hai Li, G. Crystallite size-modulated exciton emission in SnO 2 nanocrystalline films grown by sputtering. *J. Appl. Phys.* **2013**, *113*, 143104, doi:10.1063/1.4800896.
6. Kolmakov, a; Zhang, Y.; Cheng, G.; Moskovits, M. Detection of CO and O2 Using Tin Oxide Nanowire Sensors. *Adv. Mater.* **2003**, *15*, 997–1000.
7. Wang, Z.L. Functional oxide nanobelts: materials, properties and potential applications in nanosystems and biotechnology. *Annu. Rev. Phys. Chem.* **2004**, *55*, 159–96.
8. Wan, Q.; Wang, T.H. Single-crystalline Sb-doped SnO2 nanowires: synthesis and gas sensor application. *Chem. Commun.* **2005**, 3841, doi:10.1039/b504094a.

9. Amorim, C.A.; Dalmaschio, C.J.; Melzi, A.L.R.; Leite, E.R.; Chiquito, A.J. Weak localization and electron-electron scattering in fluorine-doped SnO2 random nanobelt thin films. *J. Phys. Chem. Solids* **2014**, *75*, doi:10.1016/j.jpcs.2014.01.003.
10. Martinez, A.I.; Acosta, D.R. Effect of the fluorine content on the structural and electrical properties of SnO and ZnO-SnO thin films prepared by spray pyrolysis. *Thin Solid Films* **2005**, *483*, 107–113.
11. Sun, J.; Lu, A.; Wang, L.; Hu, Y.; Wan, Q. High-mobility transparent thin-film transistors with an Sb-doped SnO2 nanocrystal channel fabricated at room temperature. *Nanotechnology* **2009**, *20*, 335204.
12. Wang, Y.; Jiang, N.; Pan, D.; Jiang, H.; Hu, Y.; Li, C. Controllable oxygen vacancy SnO2-x anodes for lithium-ion batteries with high stability. *Chem. Eng. J.* **2022**, *437*, 135422, doi:10.1016/j.cej.2022.135422.
13. Pinto, A.H.; Nogueira, A.E.; Dalmaschio, C.J.; Frigini, I.N.; de Almeida, J.C.; Ferrer, M.M.; Berengue, O.M.; Gonçalves, R.A.; de Mendonça, V.R. Doped Tin Dioxide (d-SnO2) and Its Nanostructures: Review of the Theoretical Aspects, Photocatalytic and Biomedical Applications. *Solids* **2022**, *3*, 327–360, doi:10.3390/solids3020024.
14. Kong, Y.; Li, Y.; Cui, X.; Su, L.; Ma, D.; Lai, T.; Yao, L.; Xiao, X.; Wang, Y. SnO2 nanostructured materials used as gas sensors for the detection of hazardous and flammable gases: A review. *Nano Mater. Sci.* **2021**, doi:10.1016/j.nanoms.2021.05.006.
15. Wagner, R.S.; Ellis, W.C. Vapor-Liquid-Solid Mechanism of Single Crystal Growth. *Appl. Phys. Lett.* **1964**, *4*, 89.
16. Kim, D.-W.; Hwang, I.-S.; Kwon, S.J.; Kang, H.-Y.; Park, K.-S.; Choi, Y.-J.; Choi, K.-J.; Park, J.-G. Highly conductive coaxial SnO2-In2O3 heterostructured nanowires for Li ion battery electrodes. *Nano Lett.* **2007**, *7*, 3041–5, doi:10.1021/nl0715037.
17. Jakob, M.H.; Dong, B.; Gutsch, S.; Chatelle, C.; Krishnaraja, A.; Weber, W.; Zacharias, M. Label-free SnO2 nanowire FET biosensor for protein detection. *Nanotechnology* **2017**, doi:10.1088/1361-6528/aa7015.
18. Amorim, C.A.; Blanco, K.C.; Costa, I.M.; Vicente, E.F.; da S Petruci, J.F.; Contiero, J.; Leite, E.R.; Chiquito, A.J. Active-electrode biosensor of SnO 2 nanowire for cyclodextrin detection from microbial enzyme. *Nanotechnology* **2020**, *31*, 165501, doi:10.1088/1361-6528/ab5bd7.
19. Rassas, I.; Braiek, M.; Bonhomme, A.; Bessueille, F.; Raffin, G.; Majdoub, H.; Jaffrezic-Renault, N. Highly Sensitive Voltammetric Glucose Biosensor Based on Glucose Oxidase Encapsulated in a Chitosan/Kappa-Carrageenan/Gold Nanoparticle Bionanocomposite. *Sensors* **2019**, *19*, 154, doi:10.3390/s19010154.
20. Miertuš, S.; Katrlík, J.; Pizzariello, A.; Miroslav Stred'Anský; Švitel, J.; Švorc, J. Amperometric biosensors based on solid binding matrices applied in food quality monitoring. *Biosens. Bioelectron.* **1998**, *13*, 911–923, doi:10.1016/S0956-5663(98)00063-3.
21. Liu, X.; Cheng, S.; Liu, H.; Hu, S.; Zhang, D.; Ning, H. A survey on gas sensing technology. *Sensors (Switzerland)* 2012.
22. Na, C.W.; Woo, H.-S.; Kim, I.-D.; Lee, J.-H. Selective detection of NO 2 and C 2 H 5 OH using a Co 3 O 4-decorated ZnO nanowire network sensor. *Chem. Commun.* **2011**, *47*, 5148–5150.
23. Cheng, Y.; Chen, K.-S.; Meyer, N.L.; Yuan, J.; Hirst, L.S.; Chase, P.B.; Xiong, P. Functionalized SnO2 nanobelt field-effect transistor sensors for label-free detection of cardiac troponin. *Biosens. Bioelectron.* **2011**, *26*, 4538–44, doi:10.1016/j.bios.2011.05.019.
24. Jeong, S.H.; Kim, S.; Cha, J.; Son, M.S.; Park, S.H.; Kim, H.Y.; Cho, M.H.; Whangbo, M.H.; Yoo, K.H.; Kim, S.J. Hydrogen sensing under ambient conditions using SnO2 nanowires: Synergetic effect of Pd/Sn codeposition. *Nano Lett.* **2013**, *13*, 5938–5943, doi:10.1021/nl402998g.
25. Karthik, T.; Olvera, M.; Maldonado, A.; Gómez Pozos, H. CO Gas Sensing Properties of Pure and Cu-Incorporated SnO2 Nanoparticles: A Study of Cu-Induced Modifications. *Sensors* **2016**, *16*, 1283, doi:10.3390/s16081283.
26. Memon, A.F.; Ameen, S.; Qambrani, N.; Buledi, J.A.; Khand, N.H.; Solangi, A.R.; Taqvi, S.I.H.; Karaman, C.; Karimi, F.; Afsharmanesh, E. An improved electrochemical sensor based on triton X-100 functionalized SnO2 nanoparticles for ultrasensitive determination of cadmium. *Chemosphere* **2022**, *300*, 134634.
27. Lin, C.; Xu, Z.; Kong, X.; Zheng, H.; Geng, Z.; Zeng, J. Lysine-Functionalized SnO2 for Efficient CO2 Electroreduction into

Formate. *ChemNanoMat* **2022**, e202200020.

28. Wang, D.; Chen, Y.; Liu, Z.; Li, L.; Shi, C.; Qin, H.; Hu, J. CO2-sensing properties and mechanism of nano-SnO2 thick-film sensor. *Sensors Actuators B Chem.* **2016**, *227*, 73–84.
29. Zhang, D.; Liu, A.; Chang, H.; Xia, B. Room-temperature high-performance acetone gas sensor based on hydrothermal synthesized SnO 2-reduced graphene oxide hybrid composite. *Rsc Adv.* **2015**, *5*, 3016–3022.
30. de Araújo, E.P.; Amorim, C.A.; Arantes, A.N.; Chiquito, A.J. A label-free Acetone based SnO2 nanowire network sensor at room temperature. *Appl. Phys. A* **2022**, *128*, 1–8.
31. Van Hieu, N.; Khoang, N.D.; Minh, N.T.; Trung, T.; Chien, N.D. A facile thermal evaporation route for large-area synthesis of tin oxide nanowires: characterizations and their use for liquid petroleum gas sensor. *Curr. Appl. Phys.* **2010**, *10*, 636–641.
32. Liu, Z.H.; Zhang, M.; Wang, W.Q.; Wang, W.H.; Chen, J.L.; Wu, G.H.; Meng, F.B.; Liu, H.Y.; Liu, B.D.; Qu, J.P. Magnetic properties and martensitic transformation in quaternary Heusler alloy of NiMnFeGa. *J. Appl. Phys.* **2002**, *92*, 5006–5010.
33. de Araújo, E.P.; Arantes, A.N.; Costa, I.M.; Chiquito, A.J. Reliable Tin dioxide based nanowire networks as ultraviolet solar radiation sensors. *Sensors Actuators A Phys.* **2020**, *302*, 111825, doi:10.1016/j.sna.2019.111825.
34. Amorim, C.A.; Blanco, K.C.; Costa, I.M.; de Araújo, E.P.; Arantes, A. do N.; Contiero, J.; Chiquito, A.J. A New Possibility for Fermentation Monitoring by Electrical Driven Sensing of Ultraviolet Light and Glucose. *Biosensors* **2020**, *10*, 97.
35. Tripkovic, V.; Vanin, M.; Karamad, M.; Björketun, M.E.; Jacobsen, K.W.; Thygesen, K.S.; Rossmeisl, J. Electrochemical CO2 and CO reduction on metal-functionalized porphyrin-like graphene. *J. Phys. Chem. C* **2013**, doi:10.1021/jp306172k.
36. Hoa, N.D.; Van Tong, P.; Van Duy, N.; Dao, T.D.; Chung, H. V; Nagao, T.; Van Hieu, N. Effective decoration of Pd nanoparticles on the surface of SnO2 nanowires for enhancement of CO gas-sensing performance. *J. Hazard. Mater.* **2014**, *265*, 124–132.
37. Van Hieu, N. Comparative study of gas sensor performance of SnO2 nanowires and their hierarchical nanostructures. *Sensors Actuators B Chem.* **2010**, *150*, 112–119.
38. Gonzalez, D.M.R.; Kumar, Y.; Ramón, J.A.R.; Bogyreddy, N.K.R.; Olive-Méndez, S.F.; Karthik, T.V.K.; Becerra, D.; Pérez-Tijerina, E.; Agarwal, V. CO2 sensing performance enhanced by Pt-catalyzed SnO2/porous-silicon hybrid structures. *Sensors Int.* **2022**, *3*, 100165.
39. Kim, H.-J.; Lee, J.-H. Highly sensitive and selective gas sensors using p-type oxide semiconductors: Overview. *Sensors Actuators B Chem.* **2014**, *192*, 607–627, doi:10.1016/j.snb.2013.11.005.
40. Hahn, S..; Bârsan, N.; Weimar, U.; Ejakov, S..; Visser, J..; Soltis, R.. CO sensing with SnO2 thick film sensors: role of oxygen and water vapour. *Thin Solid Films* **2003**, *436*, 17–24, doi:10.1016/S0040-6090(03)00520-0.
41. Meng, L.; Jin, J.; Yang, G.; Lu, T.; Zhang, H.; Cai, C. Nonenzymatic electrochemical detection of glucose based on palladium-single-walled carbon nanotube hybrid nanostructures. *Anal. Chem.* **2009**, *81*, 7271–7280, doi:10.1021/ac901005p.
42. Feng, P.; Shao, F.; Shi, Y.; Wan, Q. Gas sensors based on semiconducting nanowire field-effect transistors. *Sensors (Basel).* **2014**, *14*, 17406–17429, doi:10.3390/s140917406.
43. Hung, C.M.; Le, D.T.T.; Van Hieu, N. On-chip growth of semiconductor metal oxide nanowires for gas sensors: A review. *J. Sci. Adv. Mater. Devices* **2017**, *2*, 263–285, doi:10.1016/j.jsamd.2017.07.009.
44. Zeng, H.; Zhang, G.; Nagashima, K.; Takahashi, T.; Hosomi, T.; Yanagida, T. Metal–oxide nanowire molecular sensors and their promises. *Chemosensors* **2021**, *9*, 41.
45. Suematsu, K.; Ma, N.; Watanabe, K.; Yuasa, M.; Kida, T.; Shimanoe, K. Effect of Humid Aging on the Oxygen Adsorption in SnO2 Gas Sensors. *Sensors* **2018**, *18*, 254, doi:10.3390/s18010254.
46. Suematsu, K.; Watanabe, K.; Yuasa, M.; Kida, T.; Shimanoe, K. Effect of Ambient Oxygen Partial Pressure on the Hydrogen Response of SnO 2 Semiconductor Gas Sensors. *J. Electrochem. Soc.* **2019**, *166*, B618–B622, doi:10.1149/2.1391906jes.
47. Xiong, Y.; Xue, Q.; Ling, C.; Lu, W.; Ding, D.; Zhu, L.; Li, X. Effective CO2 detection based on LaOCl-doped SnO2 nanofibers:

 doi:10.20944/preprints202208.0281.v1

Insight into the role of oxygen in carrier gas. *Sensors Actuators B Chem.* **2017**, *241*, 725–734, doi:10.1016/j.snb.2016.10.143.

48. Kim, J.-H.; Mirzaei, A.; Woo Kim, H.; Wu, P.; Kim, S.S. Design of supersensitive and selective ZnO-nanofiber-based sensors for H2 gas sensing by electron-beam irradiation. *Sensors Actuators B Chem.* **2019**, *293*, 210–223, doi:10.1016/j.snb.2019.04.113.
49. Wang, W.-C.; Lai, C.-Y.; Lin, Y.-T.; Yua, T.-H.; Chen, Z.-Y.; Wu, W.-W.; Yeh, P.-H. Surface defect engineering: gigantic enhancement in the optical and gas detection ability of metal oxide sensor. *RSC Adv.* **2016**, *6*, 65146–65151, doi:10.1039/C6RA09033H.